

Electronic band splittings across the antiferromagnetic phase transition of exfoliated MnPS₃ probed by μ -ARPES

Jeff Strasdass,¹ Benjamin Pestka,¹ Milosz Rybak,² Adam K. Budniak,³ Niklas Leuth,¹ Honey Boban,⁴ Vitaliy Feyer,⁴ Iulia Cojocariu,⁴ Daniel Baranowski,⁴ José Avila,⁵ Pavel Dudin,⁵ Yaron Amouyal,⁶ Lukasz Plucinski,⁴ Efrat Lifshitz,³ Magdalena Birowska,⁷ and Markus Morgenstern¹

¹*II. Institute of Physics B and JARA-FIT, RWTH-Aachen University, 52074 Aachen, Germany*

²*Department of Semiconductor Materials Engineering Faculty of Fundamental Problems of Technology Wrocław University of Science and Technology Wybrzeże Wyspińskiego 27, 50-370 Wrocław, Poland*

³*Schulich Faculty of Chemistry, Solid State Institute, Russell Berrie Nanotechnology Institute and Helen Diller Quantum Center, Technion – Israel Institute of Technology, Haifa 3200003, Israel*

⁴*Forschungszentrum Jülich, Peter Grünberg Institute (PGI-6), 52428 Jülich, Germany*

⁵*Synchrotron-SOLEIL, Université Paris-Saclay, Saint-Aubin, BP48, Paris, F91192, Gif sur Yvette, France*

⁶*Department of Materials Science and Engineering, Technion – Israel Institute of Technology, Haifa 3200003, Israel*

⁷*Institute of Theoretical Physics, Faculty of Physics, University of Warsaw, Pasteura St. 5, 02-093 Warsaw, Poland*

(Dated: November 11, 2022)

Exfoliated magnetic 2D materials provide access to a versatile tuning of magnetization properties, e.g., by gating and by proximity-induced exchange interactions with other types of 2D materials. However, the electronic band structure after exfoliation has not been probed for such materials yet, mostly due to their photochemical sensitivity. Here, we provide micron-scale angle-resolved photoelectron spectroscopy of the exfoliated intralayer antiferromagnet MnPS₃ above and below the Néel temperature in comparison with density functional theory calculations. We demonstrate a significant splitting of parts of the Mn 3d_{z²}-bands induced by the antiferromagnetic ordering. Related changes of adjacent S 3p-bands indicate a competing contribution of a ferromagnetic superexchange. The novel access to the electronic band structure is likely transferable to other MPX₃ materials (M: transition metal, P: phosphorus, X: chalcogenide) that provide a multitude of antiferromagnetic arrangements.

Corresponding author: M. Morgenstern, email: mmorgens@physik.rwth-aachen.de

I. INTRODUCTION

The first successful exfoliation of CrI₃ [1], Cr₂Ge₂Te₆ [2] and other layered magnetic materials [3–7] added ferro- and antiferromagnets to the toolbox of exfoliation-based heterostructures [8]. This enabled several magnetoelectric effects such as deliberate gate tuning of the spin-flop transition [9, 10] as well as from antiferro- to ferrimagnetism [11] or from ferro- to paramagnetism [12]. Moreover, the exchange coupling of the ferromagnet could be successfully transferred via proximity to neighboring 2D materials [13] such as graphene [14–16], WSe₂ [17], the topological insulator WTe₂ [18] and the superconductor NbSe₂ [19–21]. Recently, also twisted layers of 2D antiferromagnets have been prepared exhibiting distinct magnetic properties from their regularly stacked counterparts [22–24].

Nevertheless, the basic electronic band structure of exfoliated 2D magnetic materials has never been probed. This is most likely due to the extreme photochemical

sensitivity of most of the flakes [25]. Previous angularly resolved photoelectron spectroscopy (ARPES) data have only been obtained on in-situ cleaved bulk materials [26–34] or in-situ after molecular beam epitaxy [35]. For this reason, the interesting class of intralayer antiferromagnetic insulators XPS₃ (X = Mn, Fe, Co, Ni) [36–38] that feature rather strong magnetoelastic [39, 40], magnetoelectric [41–45] and magnetically induced electron-phonon [46] couplings have not been examined, since their large band gaps prohibit ARPES of cleaved crystals below the Néel temperature [47].

Here, we investigate exfoliated MnPS₃, an intralayer antiferromagnet (AFM) with a honeycomb-type Néel order of Mn²⁺ ions [48] and easy axis tilted by 8° from the out-of-plane direction [41] (Fig. 1a). The intralayer AFM order persists down to a monolayer [39, 49–51]. The interlayer interaction is weakly ferromagnetic [52] breaking inversion symmetry and, hence, enabling magnetoelectric (ME) coupling [43]. A sizable linear magnetoelectric coupling has indeed been found by neutron diffraction [41] and second harmonic generation [43, 53] enabling the imaging of AFM domains ($\sim 100 \mu\text{m}$) [54] and the determination of the critical exponent $\beta = 0.37$ [43]. The Néel temperature of the bulk material is $T_N = 78 \text{ K}$ [55]. Close

to the Néel temperature, the anisotropy likely changes to an in-plane XY-type AFM order [56]. The optical band gap of MnPS₃ is 2.94 eV at $T = 5$ K [57, 58] with additional localized inter-d-level transitions at lower excitation energies [57]. Weak interlayer van-der-Waals binding with energy density 0.25 J/m² (graphene: 0.38 J/m²) enables exfoliation [58].

Here, we employ such exfoliation down to single layers onto a Au/Ti-covered Si/SiO₂ substrate to probe the insulating material by μ -ARPES above and below T_N . We find a pronounced splitting of an occupied 3d_{z²} type Mn band for thicker flakes as identified by comparison with density functional theory (DFT+U) calculations. The splitting exhibits a dispersion along the k_z direction. An additional sulfur band of 3p_z type character also changes across T_N witnessing the influence of superexchange. The band structure below T_N is only slightly different for 4 layers, but strongly different for a single layer. By comparison with DFT+U calculations, we conjecture that this difference is due to strain that appears on the relatively rough surface.

II. EXPERIMENTAL DETAILS

MnPS₃ (manganese phosphorus trisulfide) was synthesized in a quartz tube via vapor transport synthesis (VTS) – without any transporting agent, i.e. no iodine was used [59, 60]. One gram of an elements mixture of metal manganese powder (Alfa Aesar), red phosphorus (Riedel-de Haën), and sulfur (Sigma-Aldrich) with atomic ratio Mn : P : S = 1 : 1 : 3 was grounded in an agate mortar. The mixture was moved into a quartz ampoule, evacuated to a high vacuum (below $4.5 \cdot 10^{-5}$ mbar) with a turbomolecular pump, and then closed by a flamer. The sealed ampoule was placed inside a previously warmed 3-zone furnace, calibrated in the way that the mixture of elements (substrate zone) was kept at 650° C and the deposition zone was at 600° C. After 5 days the furnace was turned off and the sample was left to cool down inside. Then the ampoule was opened and only recrystallized MnPS₃ from the deposition zone was collected.

As substrate for the exfoliation, we use a thin Au/Ti film that has been evaporated on a Si/SiO₂ surface (SiO₂ thickness: 90 nm) in ultrahigh vacuum (UHV) at a substrate temperature of 300 K. Directly before the exfoliation, the substrate is exposed to plasma ashing using O₂ at 300 K with a power of 50 W and a flux of 100 sccm for 25 s. Afterward, exfoliation of MnPS₃ has been performed in a clean-room environment using the scotch tape method. Best yields are obtained within 10 min directly after plasma ashing. The samples with

exfoliated flakes are initially characterized by optical microscopy and atomic force microscopy (AFMi) in tapping mode using a commercial Bruker system. Flakes of various thicknesses with clean surfaces are then investigated by μ -ARPES and X-ray photoelectron spectroscopy (XPS) at the NanoESCA beamline of Elettra, the Italian synchrotron radiation facility, using a FOCUS NanoESCA photoemission electron microscope (PEEM) in the k space mapping mode operation [61]. The PEEM is operating at a background pressure $p < 5^{-11}$ mbar. The photoelectron signal at various photon energies $h\nu$ is collected from a spot size with diameter of 5 – 10 μ m. The geometry of incident light (p-polarized) is sketched in Fig. 3a. Before the experiment, the samples are annealed at $T = 200^\circ$ C for 60 min. During the μ -ARPES experiments, the total energy resolution of beamline and analyser is 50 meV and the sample temperature is measured by a Si diode (Lake shore cryotronics). The Fermi level is determined on the Au substrate, while the work function of MnPS₃ is deduced from the onset energy of secondary electrons to be 5.45 eV independent of T .

For the sake of better visibility, we display the curvature of the measured photoelectron intensity with respect to energy. All discussed features are cross-checked to be visible in the original plots of photoelectron intensity. (Supplementary Information).

III. COMPUTATIONAL DETAILS

The bandstructure calculations are performed within the framework of the Density Functional Theory (DFT) implemented in VASP software [62, 63]. The PAW pseudopotentials [64, 65] and Perdew-Burke-Ernzerhof (PBE) exchange-correlation functional are used [66]. The kinetic energy cutoff for the plane-wave expansion is set to 500 eV. A \mathbf{k} -mesh of $10 \times 10 \times 9$ ($10 \times 10 \times 2$ and $10 \times 6 \times 2$) is taken to sample an irreducible first Brillouin zone of the primitive bulk cell (primitive and rectangular planar cell of a monolayer, respectively). We employ the GGA+U formalism proposed by Dudarev [67] to properly account for on-site Coulomb repulsion between 3d electrons of Mn ions, by using effective Hubbard U parameters. The lattice parameters and position of the atoms are fully optimized within this approach assuming the magnetic state of AFM-Néel type. The convergence criteria for the energy and force are set to 10^{-5} eV and 10^{-3} eV/Å, respectively. In the case of the monolayer, we added 20 Å of vacuum to avoid the spurious interaction between periodic replicas. The non-local nature of dispersive forces, crucial for layered materials [68–70] are accounted for

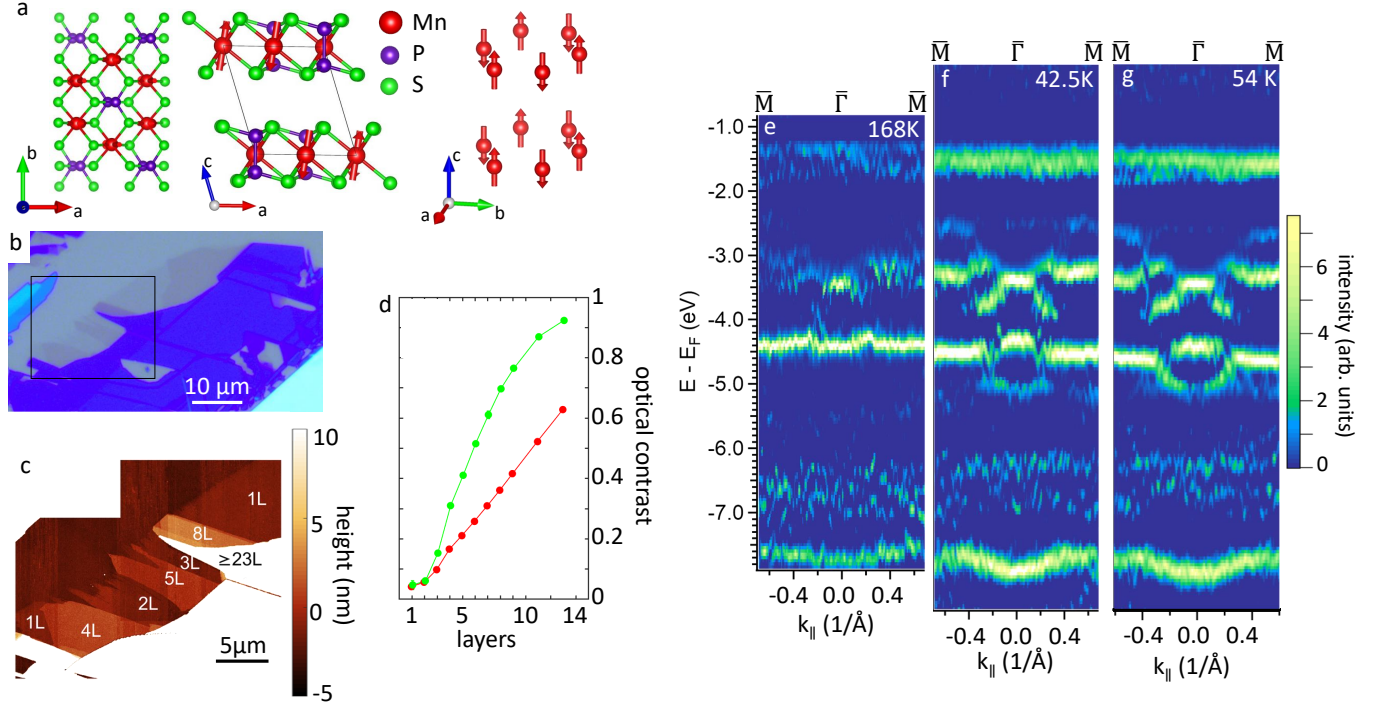


Figure 1. (a) Crystal and magnetic structure model of MnPS₃ with Mn magnetic moments depicted as arrows. Left: top view, middle: side view of two layers, right: perspective view with Mn atoms only. (b) Optical microscope image of a thick flake (violet) with several few-layer flakes at the upper left rim (darker grey areas). (c) Tapping-mode atomic force microscopy (AFMi) image of the highlighted area in b with layer thicknesses marked. (d) Optical contrast of flakes with respect to the substrate as a function of flake thickness. The green and red color filters of a Leica DFC 450 camera are used for the symbols of respective colors. The layer thicknesses are determined by AFMi. Error bars are smaller than the symbol size. (e-f) Curvature plots derived from ARPES data for exfoliated 62 layer thick MnPS₃ measured at the temperatures marked, $h\nu = 50$ eV. The Néel temperature is $T_N = 78$ K.

within semi-empirical Grimme approach [71] with a D3 parametrization [72].

IV. RESULTS

Figure 1a displays the crystal and magnetic structure of MnPS₃, the visualization was produced by using the VESTA program [73]. The Mn atoms exhibit a honeycomb lattice with a P dumbbell in the honeycomb center. Layers of S atoms on both sides terminate the single layers that are stacked by van-der-Waals forces [55]. The S atoms bridge adjacent Mn atoms, hence they contribute to their exchange path [74]. The Mn atoms show a Néel type antiferromagnetic order coupled weakly ferromagnetically between the layers. Exfoliation typically leads to relatively thick flakes with thin layers down to a monolayer at their rims (Fig. 1b-c) [58]. We found that direct

exfoliation after plasma ashing of the Au substrate provides a higher yield of thin areas, e. g. an area with a thickness of two layers and a size of $\sim 150 \times 300 \mu\text{m}^2$ (Supplementary Information). The thickness of the layers can be determined by optical contrast [54, 75] after selecting the green or red band of a standard camera (Fig. 1d) and calibrating the respective layer thicknesses by AFMi (Fig. 1c). The existence of multiple areas of different thickness at the same flake (Fig. 1c) is advantageous for its investigation by μ -ARPES with a possible focus down to $5 \mu\text{m}$ [76]. Figure 1e-g shows the measured band structure of a thicker sample area along the $\bar{M}\bar{\Gamma}\bar{M}$ direction for three different temperatures below and above $T_N = 78$ K at the identical spot (not displayed in Fig. 1 b-c). The bands at $E - E_F = -3$ eV to -5.5 eV exhibit additional substructure below T_N .

Most strikingly, there is a pronounced splitting of the lower energy band around $\bar{\Gamma}$ below T_N , but not above T_N .

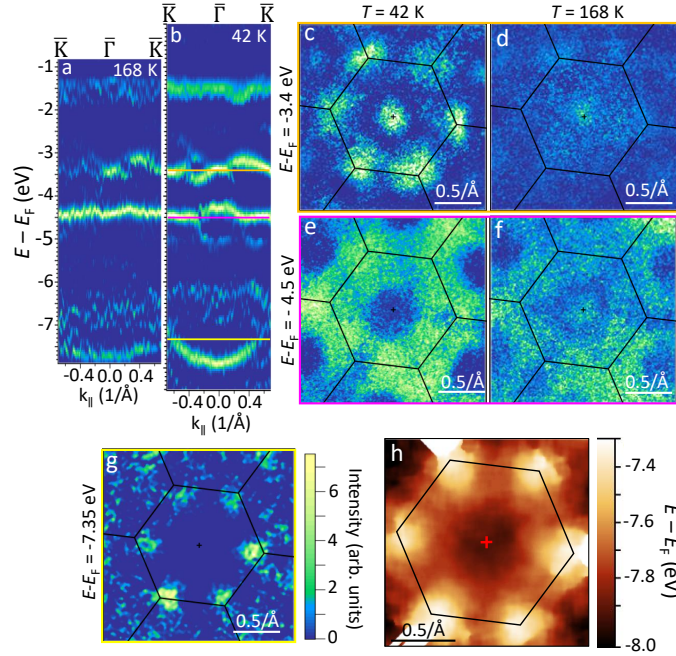


Figure 2. (a), (b) ARPES data along the $\overline{K\Gamma K}$ direction at the marked temperatures above and below $T_N = 78$ K, $h\nu = 50$ eV, 62 layers. The energies of the (k_x, k_y) maps in c-g are indicated by lines colored as the surrounding rectangles of c-g. (c), (d) Constant energy (k_x, k_y) plot of ARPES curvature intensity at $E - E_F = -3.4 \pm 0.05$ eV, $h\nu = 50$ eV, T as marked on top, 62 layers. The 2D Brillouin zone pattern of MnPS_3 is overlaid (black lines). (e), (f) Same as c, d for $E - E_F = -4.5 \pm 0.05$ eV. (g) Same as c-f at $E - E_F = -7.35 \pm 0.1$ eV, $T = 42$ K. The color bar for intensity applies to a-g. (h) Color plot of the binding energy of the lowest energy band visible in b, $h\nu = 53.5$ eV, $T = 42$ K. Lowest order 2D Brillouin zone (black) and $\overline{\Gamma}$ point (red cross) are marked. The energies are determined by the maximum of the curvature of $I(E)$ for each (k_x, k_y) using the energy interval $E - E_F = -5$ eV to -9 eV.

This also changes the propagation of the corresponding upper energy branch showing a maximum at $\overline{\Gamma}$ below T_N . Moreover, two branches declining with $|k_{\parallel}|$ get apparent at $E - E_F \simeq -3.6$ eV below T_N (ARPES at additional T in Supplementary Information). Generally, the change of the upper band at $E - E_F = -3$ eV to -3.8 eV is more subtle. There is also a small upwards shift of the most pronounced feature around $\overline{\Gamma}$ below T_N . These band changes are reproduced in several cool-downs for two thicker flakes consisting of 62 layers and 13 layers, respectively.

Figure 2 shows the measured band structure along the $\overline{K\Gamma K}$ direction (Fig. 2a,b) as well as (k_x, k_y) cuts at se-

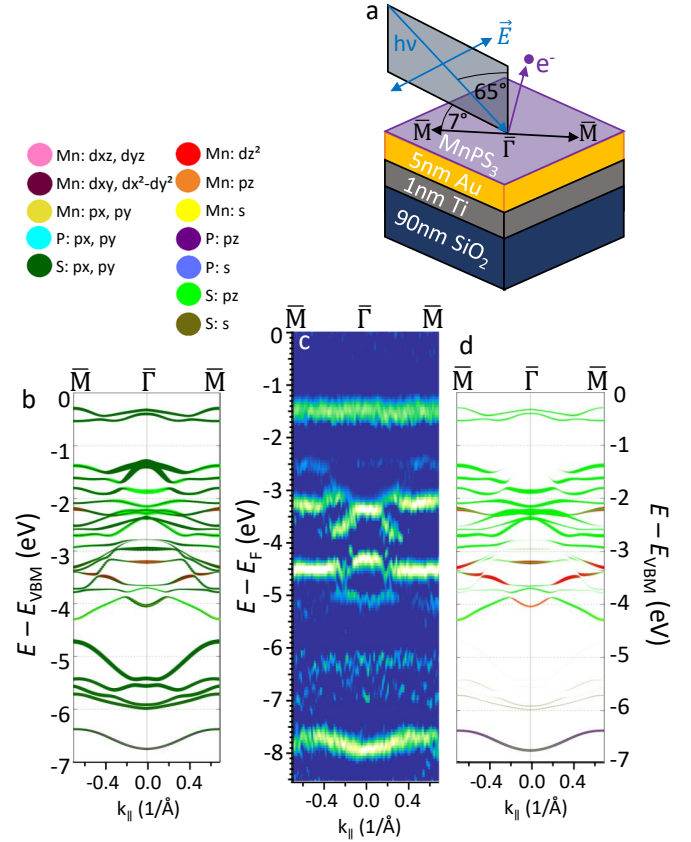


Figure 3. (a) Sketch of the sample sequence (on top of a Si substrate) and the photon beam geometry with respect to the $\overline{M\Gamma M}$ direction including the polarization direction \vec{E} . (b) Calculated band structure along the $\overline{M\Gamma M}$ direction of antiferromagnetic bulk MnPS_3 by DFT+U. $U = 1.2$ eV is deduced from a detailed comparison with the measured energy distance between the valence band maximum and the parabolic band at $E - E_{\text{VBM}} \simeq -7.5$ eV (Supplementary Information), $k_z = 0.05/\text{\AA}$. The electronic states are color-coded by the atomic orbital contribution with size giving the strength of this contribution. The color code is given on top. (c) Same as Fig. 1f. (d) Same calculation as b, but displaying only the s, p_z and d_{z^2} contributions as required by the photon beam geometry according to the analysis of matrix elements described in [77] (Supplementary Information).

lected energies, both above and below T_N (Fig. 2c-g). Moreover, the band energies of the lowest energy band belonging to b are displayed for the sake of comparison (Fig. 2h). The hexagonal surface Brillouin zone gets apparent by the symmetry that is found in all the (k_x, k_y) cuts. This symmetry does not change below T_N indicating the absence of back folding and, hence, corroborating the Néel type antiferromagnetic arrangement [48].

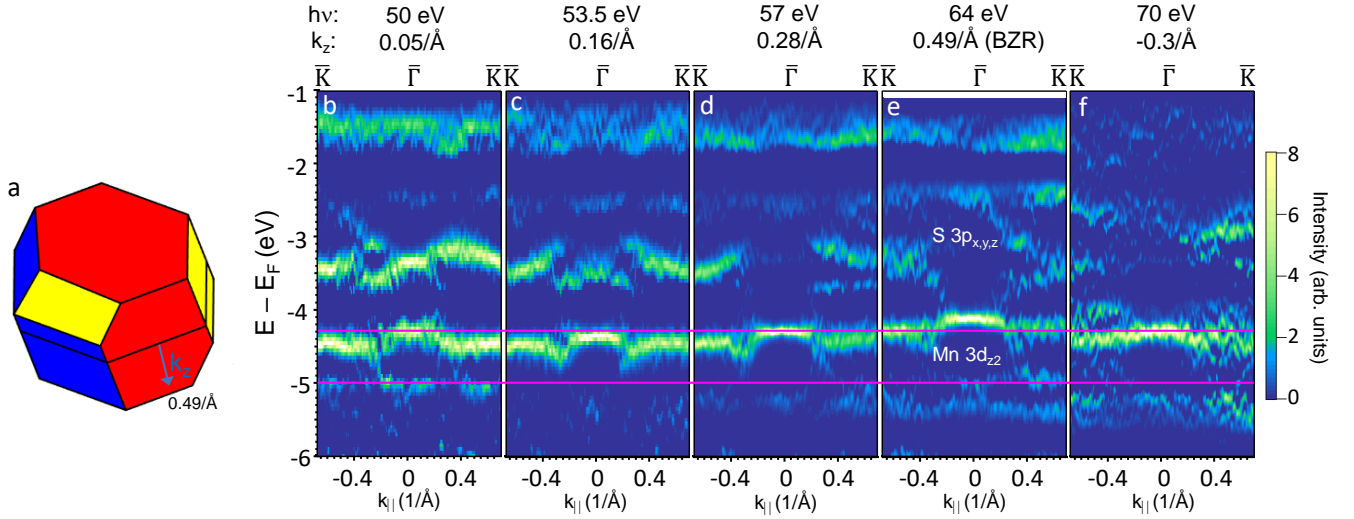


Figure 4. (a) 3D Brillouin zone of MnPS₃ with the k_z direction perpendicular to the cleavage plane indicated and the Brillouin zone boundary (BZB) at $k_z = 0.49/\text{\AA}$ marked. (b)–(f) ARPES curvature intensity along $\bar{K}\Gamma\bar{K}$ for various $h\nu$ as marked on top, $T = 42$ K, 62 layers. The indicated k_z values originate from the detailed comparison of DFT+U and ARPES data leading to Fig. 3. This implies an inner potential $V_0 = 18.6$ eV that is used straightforwardly to determine k_z assuming a final state parabola with bare electron mass (Supplementary Information). The horizontal red lines simplify the comparison between bands at different k_z . Orbitals are attributed according to Fig. 3. The increased noise for $h\nu = 70$ eV is likely caused by the fact that this $h\nu$ is far from the resonant Mn 3p excitation (Fig. 5b) [47] (Supplementary Information).

More importantly, a transition from a ring like (k_x, k_y) distribution with a local minimum in intensity at $\bar{\Gamma}$ to a structure with a local maximum at $\bar{\Gamma}$ is observed at $E - E_F = -4.5 \pm 0.05$ eV (Fig. 2e–f). This confirms the pronounced changes of this band as observed in Fig. 1e–g and Fig. 2a–b. Again, the changes of the band at slightly higher energy are more subtle (Fig. 2c–d), i.e., partly, it is hard to distinguish, if only the intensity gets significantly more pronounced below T_N or if the band propagation changes (Supplementary Information).

Figure 3 shows the comparison of the ARPES data below T_N with DFT+U calculations of the antiferromagnetic Néel structure (a, c). We used the energy of the rather parabolic sulfur band of s-type character at about $E - E_F = -7.5$ eV to calibrate $U = 1.2$ eV, since it favorably acts as a rather direct U ruler (Supplementary Information). The complete DFT band structure with marked orbital contributions is plotted in Fig. 3b. Since matrix elements in our experimental geometry (p-polarized light with incident photon beam at 65° relative to the sample normal, Fig. 3a) strongly select s-type, p_z -type and d_{z^2} -type states (Supplementary Information), we replot the DFT results with only these contributions in Fig. 3d. This selection provides a very good agreement to the experimental data and, in addition, identifies the two bands with the strongest splittings below T_N as dominated by

Mn d_{z^2} orbitals (lower energy) and S p_z orbitals (upper energy), respectively.

Figure 4 shows the k_z dispersion of the bands along the $\bar{K}\Gamma\bar{K}$ direction as probed by varying $h\nu$. We used the optimization of the agreement between experimental and DFT data to tentatively determine $k_z = 0.05/\text{\AA}$ for $h\nu = 50$ eV. Then, we propagate to higher k_z by the accordingly deduced inner potential $V_0 = 18.6$ eV (Supplementary Information). The k_{\parallel} dispersion indeed changes with k_z . This includes the size of the band splitting around $\bar{\Gamma}$ of the Mn d_{z^2} band, which increases between $h\nu = 50$ eV and $h\nu = 64$ eV (Brillouin zone boundary) as well as an upwards shift of the upper part of the Mn $3d_{z^2}$ band (see red lines in Fig. 4b–f).

The sample quality prior to and after the ARPES measurements is probed by XPS and AFMi. Figure 5a shows an overview XPS scan recorded after ARPES measurements with labeled peaks revealing the presence of O and C contamination. By comparison with the S 2p peak using peak calibration data [78, 79], we determined that the oxygen density is about 8% of the sulfur density only. The relative peak heights are the same in XPS data recorded before the ARPES measurements. This excludes that the O and C contamination originates from ARPES. Since the electron extraction area is significantly less focused for XPS ($\sim 15 \mu\text{m}$), it could be that the C and O peaks

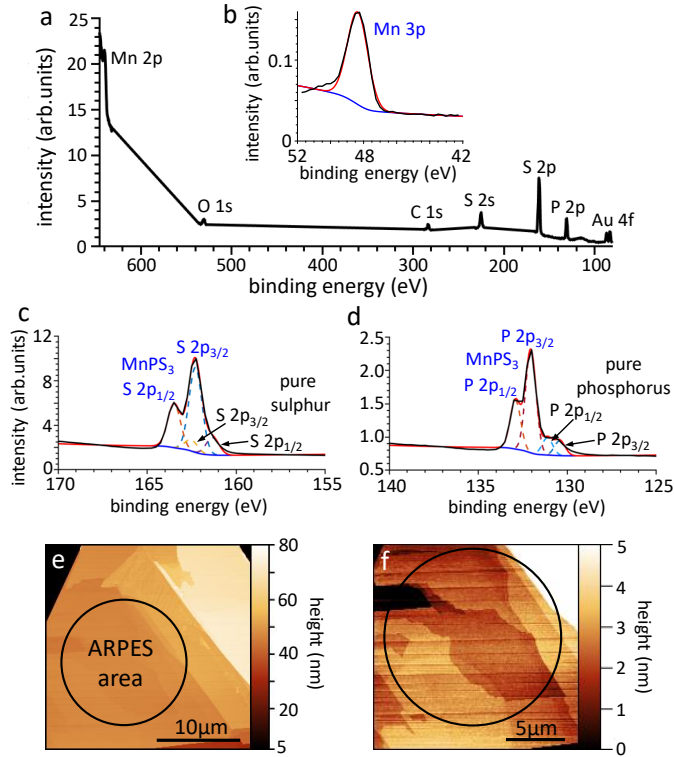


Figure 5. (a) XPS data of 13 layer MnPS_3 area recorded after extensive ARPES measurements on that area, $h\nu = 700$ eV. Peaks are labeled by chemical element and atomic orbital. A comparison of the O 1s and the S 2p peak reveals that the oxygen density is less than 8 % of the sulfur density. (b)–(d) Higher resolution XPS data of the studied 62 layer MnPS_3 area of Fig. 1–4 for the Mn 3p, S 2p and P 2p peak, respectively. Fit lines are displayed in red. They consist of the labeled dashed Lorentzian peaks and the blue Shirley–Proctor–Sherwood background. Peaks labeled blue belong to intact MnPS_3 . Peaks labeled black are likely caused by remaining intercalated pure sulfur and phosphorus from the crystal growth. (e,f) A posteriori AFM image of the area of 62 layer MnPS_3 displayed at two different scales. The area exposed to the photon beam during the ARPES measurements of Fig. 1–4 is marked. No beam damage is apparent.

are caused by remaining glue on the surface that is partially also observed by AFM. In order to reveal possible oxidation of the Mn, S and P of MnPS_3 , we fitted the corresponding peaks (Fig. 5b–d). For the S 2p and P 2p peak, we can exclude oxidation that would appear at larger binding energy (164–170 eV for S, > 134 eV for P) [80, 81]. In contrast, we observe contributions at lower binding energies that we attribute to pure S and P likely intercalated between the layers during the crystal growth. The single Mn peak (Fig. 5b) can be either caused by an

S or O induced charge transfer. Hence, we cannot exclude partial oxidation of the Mn. However, even if, this would be the case, it would only affect 8 % of the S bonds (Supplementary Information). Notice that replacement of S by O has been observed in electron microscopy, but there it is induced by the high energy electrons that kick off the S atoms prior to oxidation [82, 83].

The AFM data of the spot area of the photon beam recorded after ARPES (Fig. 5e–f) exhibit the same flatness of the surfaces as prior to ARPES.

Eventually, we also probed thinner layers (Fig. 6c,d), albeit the DFT+U calculations did not imply strong changes in the band structure (Supplementary Information). Nevertheless, we found that the energy splittings are less pronounced for a thickness of 4 layers (Fig. 6c) and, for the probed monolayer, the band structure changes significantly, appearing much more blurry than for thicker layers (Fig. 6d). This blurring is most likely related to the corrugation of the thinner MnPS_3 areas on top of the relatively rough Au/SiO₂ substrate (Fig. 6i). The substrate roughness ($\sigma = 0.33$ nm) is indeed fully transferred to the MnPS_3 monolayer ($\sigma = 0.43$ nm, Fig. 6h) and still significant for the four-layer areas ($\sigma = 0.19$ nm, Fig. 6g). In contrast, thick MnPS_3 as probed in Figs. 1–4 is rather flat (Fig. 6f, $\sigma = 0.14$ nm).

A possible explanation for the blurred ARPES data could be a local variation of the $\bar{\Gamma}$ point direction along the surface. To check this possibility, we used the spectrum of the thick film and overlapped correspondingly tilted spectra according to the measured angular distribution of the surface normal of the one-layer area (Fig. 6b) (Supplementary Information). However, this effect barely changes the measured band structure. Another possibility is the relatively strong strain in the outer sulfur layers due to the strong bending of the thin films while adhering to the substrate. The measured monolayer roughness implies a strain distribution with standard deviation $\sigma = 2.0\%$ (Fig. 6j). The four-layer film is still strained with a distribution of $\sigma = 0.9\%$, if one assumes the absence of mutual slips between the layers (Supplementary Information). DFT+U indeed reveals that isotropic tensile strain of up to 2.5% shifts the bands downwards by 200–300 meV (Fig. 6e). This explains the blurring of the spectroscopic data at lower thicknesses qualitatively, albeit the calculations can not be directly compared to the experimental data of the monolayer, since they are recorded above T_N . The strong influence of strain on the band structure is interesting in itself, but also calls for experiments on smoother substrates.

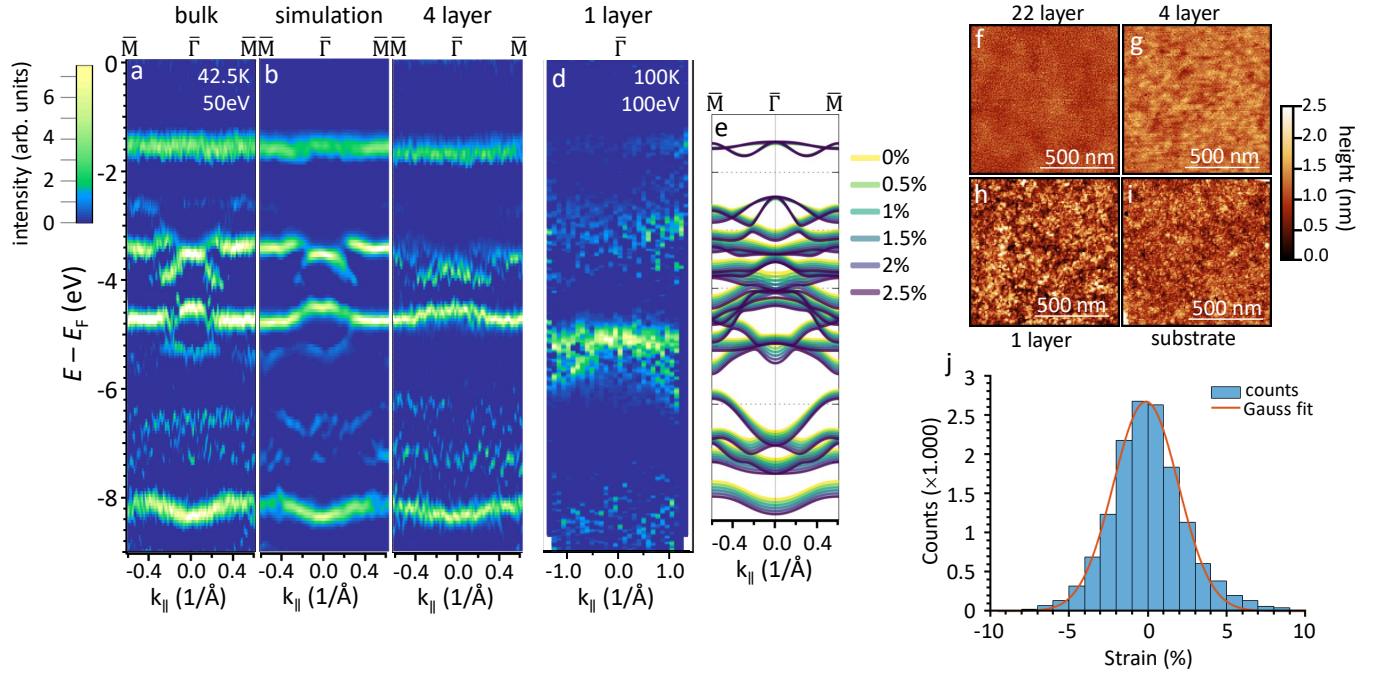


Figure 6. (a) Same as Fig. 1f. (b) Overlap of multiple spectra as in subfigure a with a Gaussian distribution of sample normals exhibiting a full width at half maximum of 2° . This distribution features the measured surface orientations of monolayer MnPS_3 exfoliated onto the Au/Ti/SiO₂/Si substrate. (c) ARPES curvature intensity along $\overline{\text{M}}\overline{\Gamma}\overline{\text{M}}$, $h\nu = 50$ eV, 4 layers, $T = 42.5$ K. (d) ARPES curvature intensity, $h\nu = 100$ eV, 1 layer, $T = 100$ K. The k_{\parallel} orientation could not be determined due to a missing clear symmetry within the (k_x, k_y) data. Note that the range on k_{\parallel} is larger than in a–c. (e) Calculated band structures along $\overline{\text{M}}\overline{\Gamma}\overline{\text{M}}$ for different isotropic tensile strains as marked, $U = 1.2$ eV, $k_z = 0.05/\text{\AA}$. (f)–(h) Tapping mode AFM images of MnPS_3 areas at different thicknesses as marked resulting in rms roughnesses: (f) $\sigma_{\text{rms}} = 1.4$ \AA, (g) $\sigma_{\text{rms}} = 1.9$ \AA, (h) $\sigma_{\text{rms}} = 4.3$ \AA. (i) Tapping mode AFM image of the Au substrate, $\sigma_{\text{rms}} = 3.3$ \AA. (j) Strain distribution resulting from the analysis of the one-layer film (Supplementary Information). A Gaussian fit (red line) with $\sigma = 2\%$ is added.

V. SUMMARY

We have demonstrated the first successful ARPES study of exfoliated magnetic 2D materials using the rather inert MnPS_3 . We found a pronounced splitting of a Mn $3d_z^2$ band while cooling below the Néel temperature and some more subtle changes of S $3p_{x,y,z}$ bands at slightly higher energies. The band orbitals are identified by comparison with DFT+U calculations, enabling in turn to determine $U \simeq 1.2$ eV. The splitting of the Mn $3d_z^2$ band also exhibits a k_z dependence. For thin films (1 layer, 4 layers), we find that the band structure appears blurred not agreeing with the unstrained DFT+U results. This effect is attributed to a spatially varying strain caused by a relatively rough substrate. This strain influence is in-

teresting in itself and could be mitigated by optimization of the substrate preparation.

The large variety of similar MPX_3 materials ($M = \text{Ni}, \text{Fe}, \text{Co}, \text{Zn}$; $X = \text{S}, \text{Se}$) as well as corresponding alloys with multiple magnetic and magnetoelectric structures [84] opens a vast field for studying band structure changes across the critical temperature of magnetic materials down to the true 2D limit. This will enable a more concise understanding of the interrelation between magnetism and electronic structure for these novel types of true 2D magnets.

VI. ACKNOWLEDGEMENT

We acknowledge financial support from the German Research Foundation (DFG) via the project Mo 858/19-1 and from the European Union's Horizon 2020 research and innovation program under grant agreement number 881603 (Graphene Flagship, Core 3). M.B. acknowledges support from the University of Warsaw within the project "Excellence Initiative-Research University" program. Access to computing facilities of PL-Grid Polish Infrastruc-

ture for Supporting Computational Science in the European Research Space and of the Interdisciplinary Center of Modeling (ICM), University of Warsaw are gratefully acknowledged. We acknowledge access to the NanoESCA beamline of Elettra, the Italian synchrotron facility. E.L. is supported by the Israel Science Foundation (project no. 2528/19) and by the Deutsche - Israel Program (project no. NA1223/2-1). A.K.B and E.F. were supported by the European Commission via the Marie-Sklodowska Curie action Phonsi (H2020-MSCA-ITN-642656).

-
- [1] B. Huang, G. Clark, E. Navarro-Moratalla, D. R. Klein, R. Cheng, K. L. Seyler, D. Zhong, E. Schmidgall, M. A. McGuire, D. H. Cobden, W. Yao, D. Xiao, P. Jarillo-Herrero, and X. Xu, *Layer-dependent ferromagnetism in a van der Waals crystal down to the monolayer limit*, Nature **546**, 270 (2017), URL <https://doi.org/10.1038/nature22391>.
- [2] C. Gong, L. Li, Z. Li, H. Ji, A. Stern, Y. Xia, T. Cao, W. Bao, C. Wang, Y. Wang, Z. Q. Qiu, R. J. Cava, S. G. Louie, J. Xia, and X. Zhang, *Discovery of intrinsic ferromagnetism in two-dimensional van der Waals crystals*, Nature **546**, 265 (2017), URL <https://doi.org/10.1038/nature22060>.
- [3] B. Huang, M. A. McGuire, A. F. May, D. Xiao, P. Jarillo-Herrero, and X. Xu, *Emergent phenomena and proximity effects in two-dimensional magnets and heterostructures*, Nat. Mater. **19**, 1276 (2020), URL <https://doi.org/10.1038/s41563-020-0791-8>.
- [4] M. Gibertini, M. Koperski, A. F. Morpurgo, and K. S. Novoselov, *Magnetic 2D materials and heterostructures*, Nat. Nanotechnol. **14**, 408 (2019), URL <https://doi.org/10.1038/s41565-019-0438-6>.
- [5] C. Gong and X. Zhang, *Two-dimensional magnetic crystals and emergent heterostructure devices*, Science **363** (2019), URL <https://doi.org/10.1126/science.aav4450>.
- [6] K. S. Burch, D. Mandrus, and J.-G. Park, *Magnetism in two-dimensional van der Waals materials*, Nature **563**, 47 (2018), URL <https://doi.org/10.1038/s41586-018-0631-z>.
- [7] Z. Fei, B. Huang, P. Malinowski, W. Wang, T. Song, J. Sanchez, W. Yao, D. Xiao, X. Zhu, A. F. May, W. Wu, D. H. Cobden, J.-H. Chu, and X. Xu, *Two-dimensional itinerant ferromagnetism in atomically thin Fe₃GeTe₂*, Nat. Mater. **17**, 778 (2018), URL <https://doi.org/10.1038/s41563-018-0149-7>.
- [8] K. S. Novoselov, A. Mishchenko, A. Carvalho, and A. H. C. Neto, *2D materials and van der Waals heterostructures*, Science **353** (2016), URL <https://doi.org/10.1126/science.aac9439>.
- [9] B. Huang, G. Clark, D. R. Klein, D. MacNeill, E. Navarro-Moratalla, K. L. Seyler, N. Wilson, M. A. McGuire, D. H. Cobden, D. Xiao, W. Yao, P. Jarillo-Herrero, and X. Xu, *Electrical control of 2D magnetism in bilayer CrI₃*, Nat. Nanotechnol. **13**, 544 (2018), URL <https://doi.org/10.1038/s41565-018-0121-3>.
- [10] S. Jiang, J. Shan, and K. F. Mak, *Electric-field switching of two-dimensional van der Waals magnets*, Nat. Mater. **17**, 406 (2018), URL <https://doi.org/10.1038/s41563-018-0040-6>.
- [11] S. Jiang, L. Li, Z. Wang, K. F. Mak, and J. Shan, *Controlling magnetism in 2D CrI₃ by electrostatic doping*, Nat. Nanotechnol. **13**, 549 (2018), URL <https://doi.org/10.1038/s41565-018-0135-x>.
- [12] Y. Deng, Y. Yu, Y. Song, J. Zhang, N. Z. Wang, Z. Sun, Y. Yi, Y. Z. Wu, S. Wu, J. Zhu, J. Wang, X. H. Chen, and Y. Zhang, *Gate-tunable room-temperature ferromagnetism in two-dimensional Fe₃GeTe₂*, Nature **563**, 94 (2018), URL <https://doi.org/10.1038/s41586-018-0626-9>.
- [13] J. F. Sierra, J. Fabian, R. K. Kawakami, S. Roche, and S. O. Valenzuela, *Van der Waals heterostructures for spintronics and opto-spintronics*, Nat. Nanotechnol. **16**, 856 (2021), URL <https://doi.org/10.1038/s41565-021-00936-x>.
- [14] Y. Wu, G. Yin, L. Pan, A. J. Grutter, Q. Pan, A. Lee, D. A. Gilbert, J. A. Borchers, W. Ratcliff, A. Li, X. dong Han, and K. L. Wang, *Large exchange splitting in monolayer graphene magnetized by an antiferromagnet*, Nat. Electron. **3**, 604 (2020), URL <https://doi.org/10.1038/s41928-020-0458-0>.
- [15] T. S. Ghiasi, A. A. Kaverzin, A. H. Dismukes, D. K. de Wal, X. Roy, and B. J. van Wees, *Electrical and thermal generation of spin currents by magnetic bilayer graphene*, Nat. Nanotechnol. **16**, 788 (2021), URL <https://doi.org/10.1038/s41565-021-00887-3>.
- [16] C. Tang, Z. Zhang, S. Lai, Q. Tan, and W. bo Gao, *Magnetic Proximity Effect in Graphene/CrBr₃ van der Waals Heterostructures*, Adv. Mater. **32**, 1908498 (2020), URL <https://doi.org/10.1002/adma.201908498>.
- [17] D. Zhong, K. L. Seyler, X. Linpeng, N. P. Wilson, T. Taniguchi, K. Watanabe, M. A. McGuire, K.-M. C. Fu, D. Xiao, W. Yao, and X. Xu, *Layer-resolved magnetic proximity effect in van der Waals heterostructures*, Nat.

- Nanotechnol. **15**, 187 (2020), URL <https://doi.org/10.1038/s41565-019-0629-1>.
- [18] W. Zhao, Z. Fei, T. Song, H. K. Choi, T. Palomaki, B. Sun, P. Malinowski, M. A. McGuire, J.-H. Chu, X. Xu, and D. H. Cobden, *Magnetic proximity and nonreciprocal current switching in a monolayer WTe₂ helical edge*, Nat. Mater. **19**, 503 (2020), URL <https://doi.org/10.1038/s41563-020-0620-0>.
- [19] K. Kang, S. Jiang, H. Berger, K. Watanabe, T. Taniguchi, L. Forró³, J. Shan, and K. F. Mak, *Giant anisotropic magnetoresistance in Ising superconductor-magnetic insulator tunnel junctions*, arXiv: p. .01327 (2021), URL <https://arxiv.org/abs/2101.01327>.
- [20] A. Hamill, B. Heischmidt, E. Sohn, D. Shaffer, K.-T. Tsai, X. Zhang, X. Xi, A. Suslov, H. Berger, L. Forró, F. J. Burnell, J. Shan, K. F. Mak, R. M. Fernandes, K. Wang, and V. S. Pribiag, *Two-fold symmetric superconductivity in few-layer NbSe₂*, Nat. Phys. **17**, 949 (2021), URL <https://doi.org/10.1038/s41567-021-01219-x>.
- [21] S. Kezilebieke, M. N. Huda, V. Vaño, M. Aapro, S. C. Ganguli, O. J. Silveira, S. Głodzik, A. S. Foster, T. Ojanen, and P. Liljeroth, *Topological superconductivity in a van der Waals heterostructure*, Nature **588**, 424 (2020), URL <https://doi.org/10.1038/s41586-020-2989-y>.
- [22] H. Xie, X. Luo, G. Ye, Z. Ye, H. Ge, S. H. Sung, E. Rennich, S. Yan, Y. Fu, S. Tian, H. Lei, R. Hovden, K. Sun, R. He, and L. Zhao, *Twist engineering of the two-dimensional magnetism in double bilayer chromium triiodide homostructures*, Nat. Phys. **18**, 30 (2021), URL <https://doi.org/10.1038/s41567-021-01408-8>.
- [23] T. Song, Q.-C. Sun, E. Anderson, C. Wang, J. Qian, T. Taniguchi, K. Watanabe, M. A. McGuire, R. Stöhr, D. Xiao, T. Cao, J. Wrachtrup, and X. Xu, *Direct visualization of magnetic domains and moiré magnetism in twisted 2D magnets*, Science **374**, 1140 (2021), URL <https://doi.org/10.1126/science.abj7478>.
- [24] Y. Xu, A. Ray, Y.-T. Shao, S. Jiang, K. Lee, D. Weber, J. E. Goldberger, K. Watanabe, T. Taniguchi, D. A. Muller, K. F. Mak, and J. Shan, *Coexisting ferromagnetic-antiferromagnetic state in twisted bilayer CrI₃*, Nat. Nanotechnol. **17**, 143 (2021), URL <https://doi.org/10.1038/s41565-021-01014-y>.
- [25] D. Shcherbakov, P. Stepanov, D. Weber, Y. Wang, J. Hu, Y. Zhu, K. Watanabe, T. Taniguchi, Z. Mao, W. Windl, J. Goldberger, M. Bockrath, and C. N. Lau, *Raman Spectroscopy, Photocatalytic Degradation, and Stabilization of Atomically Thin Chromium Tri-iodide*, Nano Lett. **18**, 4214 (2018), URL <https://doi.org/10.1021/acs.nanolett.8b01131>.
- [26] M. D. Watson, I. Marković, F. Mazzola, A. Rajan, E. A. Morales, D. M. Burn, T. Hesjedal, G. van der Laan, S. Mukherjee, T. K. Kim, C. Bigi, I. Vobornik, M. C. Hattnean, G. Balakrishnan, and P. D. C. King, *Direct observation of the energy gain underpinning ferromagnetic superexchange in the electronic structure of CrGeTe₃*, Phys. Rev. B **101**, 205125 (2020), URL <https://doi.org/10.1103/physrevb.101.205125>.
- [27] T. Yilmaz, R. M. Geilhufe, I. Pletikosić, G. W. Fernando, R. J. Cava, T. Valla, E. Vescovo, and B. Sinkovic, *Multi-hole bands and quasi-two-dimensionality in Cr₂Ge₂Te₆ studied by angle-resolved photoemission spectroscopy*, Europhys. Lett. **133**, 27002 (2021), URL <https://doi.org/10.1209/0295-5075/133/27002>.
- [28] X. Xu, Y. W. Li, S. R. Duan, S. L. Zhang, Y. J. Chen, L. Kang, A. J. Liang, C. Chen, W. Xia, Y. Xu, P. Malinowski, X. D. Xu, J.-H. Chu, G. Li, Y. F. Guo, Z. K. Liu, L. X. Yang, and Y. L. Chen, *Signature for non-Stoner ferromagnetism in the van der Waals ferromagnet Fe₃GeTe₂*, Phys. Rev. B **101**, 201104 (2020), URL <https://doi.org/10.1103/physrevb.101.201104>.
- [29] J. S. Liu, S. C. Huan, Z. H. Liu, W. L. Liu, Z. T. Liu, X. L. Lu, Z. Huang, Z. C. Jiang, X. Wang, N. Yu, Z. Q. Zou, Y. F. Guo, and D. W. Shen, *Electronic structure of the high-mobility two-dimensional antiferromagnetic metal GdTe₃*, Phys. Rev. Mat. **4**, 114005 (2020), URL <https://doi.org/10.1103/physrevmaterials.4.114005>.
- [30] Y. F. Li, W. Wang, W. Guo, C. Y. Gu, H. Y. Sun, L. He, J. Zhou, Z. B. Gu, Y. F. Nie, and X. Q. Pan, *Electronic structure of ferromagnetic semiconductor CrGeTe₃ by angle-resolved photoemission spectroscopy*, Phys. Rev. B **98**, 125127 (2018), URL <https://doi.org/10.1103/physrevb.98.125127>.
- [31] M. Suzuki, B. Gao, K. Koshiishi, S. Nakata, K. Hagiwara, C. Lin, Y. X. Wan, H. Kumigashira, K. Ono, S. Kang, S. Kang, J. Yu, M. Kobayashi, S.-W. Cheong, and A. Fujimori, *Coulomb-interaction effect on the two-dimensional electronic structure of the van der Waals ferromagnet Cr₂Ge₂Te₆*, Phys. Rev. B **99**, 161401 (2019), URL <https://doi.org/10.1103/physrevb.99.161401>.
- [32] Y. Zhang, H. Lu, X. Zhu, S. Tan, W. Feng, Q. Liu, W. Zhang, Q. Chen, Y. Liu, X. Luo, D. Xie, L. Luo, Z. Zhang, and X. Lai, *Emergence of Kondo lattice behavior in a van der Waals itinerant ferromagnet, Fe₃GeTe₂*, Sci. Adv. **4**, aao6791 (2018), URL <https://doi.org/10.1126/sciadv.aao6791>.
- [33] T. Kong, K. Stolze, E. I. Timmons, J. Tao, D. Ni, S. Guo, Z. Yang, R. Prozorov, and R. J. Cava, *V_{I3}- a New Layered Ferromagnetic Semiconductor*, Adv. Mater. **31**, 1808074 (2019), URL <https://doi.org/10.1002/adma.201808074>.
- [34] W. Jiang, Z. Yang, Y. Li, G. Wang, Q. Jing, D. Guan, J. Ma, W. Zhang, and D. Qian, *Spin-split valence bands of the ferromagnetic insulator Cr₂Ge₂Te₆ studied by angle-resolved photoemission spectroscopy*, J. Appl. Phys. **127**, 023901 (2020), URL <https://doi.org/10.1063/1.5135759>.
- [35] X. Zhang, Q. Lu, W. Liu, W. Niu, J. Sun, J. Cook, M. Vaninger, P. F. Miceli, D. J. Singh, S.-W. Lian, T.-R. Chang, X. He, J. Du, L. He, R. Zhang, G. Bian, and Y. Xu, *Room-temperature intrinsic ferromagnetism in epitaxial CrTe₂ ultrathin films*, Nat. Commun. **12** (2021), URL <https://doi.org/10.1038/s41467-021-22777-x>.
- [36] P. A. Joy and S. Vasudevan, *Magnetism in the layered transition-metal thiophosphates MPS₃ (M=Mn, Fe, and*

- Ni*), Phys. Rev. B **46**, 5425 (1992), URL <https://doi.org/10.1103/physrevb.46.5425>.
- [37] M. A. Susner, M. Chyasnaychuyus, M. A. McGuire, P. Ganesh, and P. Maksymovych, *Metal Thio- and Selenophosphates as Multifunctional van der Waals Layered Materials*, Adv. Mater. **29**, 1602852 (2017), URL <https://doi.org/10.1002/adma.201602852>.
- [38] F. Wang, T. A. Shifa, P. Yu, P. He, Y. Liu, F. Wang, Z. Wang, X. Zhan, X. Lou, F. Xia, and J. He, *New Frontiers on van der Waals Layered Metal Phosphorous Trichalcogenides*, Adv. Funct. Mater. **28**, 1802151 (2018), URL <https://doi.org/10.1002/adfm.201802151>.
- [39] D. Vaclavkova, A. Delhomme, C. Faugeras, M. Potemski, A. Bogucki, J. Suffczyński, P. Kossacki, A. R. Wildes, B. Grémaud, and A. Saúl, *Magnetoelastic interaction in the two-dimensional magnetic material MnPS₃ studied by first principles calculations and Raman experiments*, 2D Mater. **7**, 035030 (2020), URL <https://doi.org/10.1088/2053-1583/ab93e3>.
- [40] S. Liu, A. G. del Águila, D. Bhowmick, C. K. Gan, T. T. H. Do, M. Prosnikov, D. Sedmidubský, Z. Sofer, P. C. Christianen, P. Sengupta, and Q. Xiong, *Direct Observation of Magnon-Phonon Strong Coupling in Two-Dimensional Antiferromagnet at High Magnetic Fields*, Phys. Rev. Lett. **127**, 097401 (2021), URL <https://doi.org/10.1103/physrevlett.127.097401>.
- [41] E. Ressouche, M. Loire, V. Simonet, R. Ballou, A. Stunault, and A. Wildes, *Magnetolectric MnPS₃ as a candidate for ferrotoroidicity*, Phys. Rev. B **82**, 100408 (2010), URL <https://doi.org/10.1103/physrevb.82.100408>.
- [42] Y. Lai, Z. Song, Y. Wan, M. Xue, C. Wang, Y. Ye, L. Dai, Z. Zhang, W. Yang, H. Du, and J. Yang, *Two-dimensional ferromagnetism and driven ferroelectricity in van der Waals CuCrP₂S₆*, Nanoscale **11**, 5163 (2019), URL <https://doi.org/10.1039/c9nr00738e>.
- [43] H. Chu, C. J. Roh, J. O. Island, C. Li, S. Lee, J. Chen, J.-G. Park, A. F. Young, J. S. Lee, and D. Hsieh, *Linear Magnetolectric Phase in Ultrathin MnPS₃ Probed by Optical Second Harmonic Generation*, Phys. Rev. Lett. **124**, 027601 (2020), URL <https://doi.org/10.1103/physrevlett.124.027601>.
- [44] S. Y. Kim, T. Y. Kim, L. J. Sandilands, S. Sinn, M.-C. Lee, J. Son, S. Lee, K.-Y. Choi, W. Kim, B.-G. Park, C. Jeon, H.-D. Kim, C.-H. Park, J.-G. Park, S. Moon, and T. Noh, *Charge-Spin Correlation in van der Waals Antiferromagnet NiPS₃*, Phys. Rev. Lett. **120**, 136402 (2018), URL <https://doi.org/10.1103/physrevlett.120.136402>.
- [45] S. Kang, K. Kim, B. H. Kim, J. Kim, K. I. Sim, J.-U. Lee, S. Lee, K. Park, S. Yun, T. Kim, A. Nag, A. Walters, M. Garcia-Fernandez, J. Li, L. Chapon, K.-J. Zhou, Y.-W. Son, J. H. Kim, H. Cheong, and J.-G. Park, *Coherent many-body exciton in van der Waals antiferromagnet NiPS₃*, Nature **583**, 785 (2020), URL <https://doi.org/10.1038/s41586-020-2520-5>.
- [46] E. Ergeçen, B. Ilyas, D. Mao, H. C. Po, M. B. Yilmaz, J. Kim, J.-G. Park, T. Senthil, and N. Gedik, *Magnetically brightened dark electron-phonon bound states in a van der Waals antiferromagnet*, Nature Communications **13** (2022), URL <https://doi.org/10.1038/s41467-021-27741-3>.
- [47] A. Kamata, K. Noguchi, K. Suzuki, H. Tezuka, T. Kashiwakura, Y. Ohno, and S. ichi Nakai, *Resonant 2p → 3d Photoemission Measurement of MPS₃ (M=Mn, Fe, Ni)*, J. Phys. Soc. Jp. **66**, 401 (1997), URL <https://doi.org/10.1143/jpsj.66.401>.
- [48] K. Kurosawa, S. Saito, and Y. Yamaguchi, *Neutron Diffraction Study on MnPS₃ and FePS₃*, J. Phys. Soc. Jpn. **52**, 3919 (1983), URL <https://doi.org/10.1143/jpsj.52.3919>.
- [49] S. Y. Lim, K. Kim, S. Lee, J.-G. Park, and H. Cheong, *Thickness dependence of antiferromagnetic phase transition in Heisenberg-type MnPS₃*, Current Appl. Phys. **21**, 1 (2021), URL <https://doi.org/10.1016/j.cap.2020.09.017>.
- [50] K. Kim, S. Y. Lim, J. Kim, J.-U. Lee, S. Lee, P. Kim, K. Park, S. Son, C.-H. Park, J.-G. Park, and H. Cheong, *Antiferromagnetic ordering in van der Waals 2D magnetic material MnPS₃ probed by Raman spectroscopy*, 2D Mater. **6**, 041001 (2019), URL <https://doi.org/10.1088/2053-1583/ab27d5>.
- [51] G. Long, H. Henck, M. Gibertini, D. Dumcenco, Z. Wang, T. Taniguchi, K. Watanabe, E. Giannini, and A. F. Morpurgo, *Persistence of Magnetism in Atomically Thin MnPS₃ Crystals*, Nano Lett. **20**, 2452 (2020), URL <https://doi.org/10.1021/acs.nanolett.9b05165>.
- [52] T. Babuka, M. Makowska-Janusik, A. Peschanskii, K. Glukhov, S. Gnatchenko, and Y. Vysochanskii, *Electronic and vibrational properties of pure MnPS₃ crystal: Theoretical and experimental investigation*, Comp. Mater. Sci. **177**, 109592 (2020), URL <https://doi.org/10.1016/j.commatsci.2020.109592>.
- [53] J.-Y. Shan, M. Ye, H. Chu, S. Lee, J.-G. Park, L. Balents, and D. Hsieh, *Giant modulation of optical nonlinearity by Floquet engineering*, Nature **600**, 235 (2021), URL <https://doi.org/10.1038/s41586-021-04051-8>.
- [54] Z. Ni, H. Zhang, D. A. Hopper, A. V. Haglund, N. Huang, D. Jariwala, L. C. Bassett, D. G. Mandrus, E. J. Mele, C. L. Kane, and L. Wu, *Direct Imaging of Antiferromagnetic Domains and Anomalous Layer-Dependent Mirror Symmetry Breaking in Atomically Thin MnPS₃*, Phys. Rev. Lett. **127**, 187201 (2021), URL <https://doi.org/10.1103/physrevlett.127.187201>.
- [55] R. Brec, *Review on structural and chemical properties of transition metal phosphorous trisulfides MPS₃*, Solid State Ionics **22**, 3 (1986), ISSN 0167-2738.
- [56] A. R. Wildes, H. M. Rønnow, B. Roessli, M. J. Harris, and K. W. Godfrey, *Static and dynamic critical properties of the quasi-two-dimensional antiferromagnet MnPS₃*, Phys. Rev. B **74**, 094422 (2006), URL <https://doi.org/10.1103/physrevb.74.094422>.
- [57] V. Grasso, F. Neri, P. Perillo, L. Silipigni, and M. Piacentini, *Optical-absorption spectra of crystal-field transitions in MnPS₃ at low temperatures*, Phys. Rev. B **44**, 11060

- (1991), URL <https://doi.org/10.1103/physrevb.44.11060>.
- [58] K. Zhao Du, X. Zhi Wang, Y. Liu, P. Hu, M. I. B. Utama, C. K. Gan, Q. Xiong, and C. Kloc, *Weak Van der Waals Stacking, Wide-Range Band Gap, and Raman Study on Ultrathin Layers of Metal Phosphorus Trichalcogenides*, ACS Nano **10**, 1738 (2016), URL <https://doi.org/10.1021/acsnano.5b05927>.
- [59] B. E. Taylor, J. Steger, and A. Wold, *Preparation and properties of some transition metal phosphorus trisulfide compounds*, Journal of Solid State Chemistry **7**, 461 (1973), URL [https://doi.org/10.1016/0022-4596\(73\)90175-8](https://doi.org/10.1016/0022-4596(73)90175-8).
- [60] A. K. Budniak, N. A. Killilea, S. J. Zelewski, M. Sytnyk, Y. Kauffmann, Y. Amouyal, R. Kudrawiec, W. Heiss, and E. Lifshitz, *Exfoliated CrPS₄ with Promising Photoconductivity*, Small **16**, 1905924 (2020), URL <https://doi.org/10.1002/sml1.201905924>.
- [61] C. Schneider, C. Wiemann, M. Patt, V. Feyer, L. Plucinski, I. Krug, M. Escher, N. Weber, M. Merkel, O. Renault, and N. Barrett, *Expanding the view into complex material systems: From micro-ARPES to nanoscale HAXPES*, J. Electr. Spectr. Rel. Phenom. **185**, 330 (2012), URL <https://doi.org/10.1016/j.elspec.2012.08.003>.
- [62] G. Kresse and J. Hafner, *Ab initio*, Phys. Rev. B **47**, 558 (1993).
- [63] G. Kresse and J. F. Müller, *Efficiency of ab-initio total energy calculations for metals and semiconductors using a plane-wave basis set*, Computational Materials Science **6**, 15 (1996), ISSN 0927-0256.
- [64] P. E. Blochl, *Projector augmented-wave method*, Phys. Rev. B **50**, 17953 (1994).
- [65] G. Kresse and D. Joubert, *From ultrasoft pseudopotentials to the projector augmented-wave method*, Phys. Rev. B **59**, 1758 (1999).
- [66] J. P. Perdew, K. Burke, and M. Ernzerhof, *Generalized Gradient Approximation Made Simple*, Phys. Rev. Lett. **77**, 3865 (1996).
- [67] S. L. Dudarev, G. A. Botton, S. Y. Savrasov, C. J. Humphreys, and A. P. Sutton, *Electron-energy-loss spectra and the structural stability of nickel oxide: An LSDA+U study*, Phys. Rev. B **57**, 1505 (1998).
- [68] S. A. Tawfik, T. Gould, C. Stampfl, and M. J. Ford, *Evaluation of van der Waals density functionals for layered materials*, Phys. Rev. Materials **2**, 034005 (2018), URL <https://link.aps.org/doi/10.1103/PhysRevMaterials.2.034005>.
- [69] M. Birowska, K. Milowska, and J. A. Majewski, *Van Der Waals Density Functionals for Graphene Layers and Graphite*, Acta Physica Polonica A **120**, 845 (2011).
- [70] M. Birowska, M. E. Marchwiany, C. Draxl, and J. A. Majewski, *Assessment of approaches for dispersive forces employing semihydrogenated graphene as a case study*, Computational Materials Science **186**, 109940 (2021), ISSN 0927-0256, URL <https://www.sciencedirect.com/science/article/pii/S0927025620304316>.
- [71] S. Grimme, *Semiempirical GGA-type density functional constructed with a long-range dispersion correction*, J. Comput. Chem. **27**, 1787 (2006).
- [72] S. Grimme, J. Antony, S. Ehrlich, and H. Krieg, *A consistent and accurate ab initio parametrization of density functional dispersion correction (DFT-D) for the 94 elements H-Pu*, J. Chem. Phys. **132**, 154104 (2010).
- [73] K. Momma and F. Izumi, *VESTA3 for three-dimensional visualization of crystal, volumetric and morphology data*, Journal of Applied Crystallography **44**, 1272 (2011), URL <https://doi.org/10.1107/S0021889811038970>.
- [74] C. Autieri, G. Cuono, C. Noce, M. Rybak, K. M. Kotur, C. E. Agrapidis, K. Wohlfeld, and M. Birowska, *Limited Ferromagnetic Interactions in Monolayers of MPS₃ (M = Mn and Ni)*, The Journal of Physical Chemistry C **126**, 6791 (2022), ISSN 1932-7447, URL <https://doi.org/10.1021/acs.jpcc.2c00646>.
- [75] Y.-J. Sun, Q.-H. Tan, X.-L. Liu, Y.-F. Gao, and J. Zhang, *Probing the Magnetic Ordering of Antiferromagnetic MnPS₃ by Raman Spectroscopy*, J. Phys. Chem. Lett. **10**, 3087 (2019), URL <https://doi.org/10.1021/acs.jpcclett.9b00758>.
- [76] C. Wiemann, M. Patt, I. P. Krug, N. B. Weber, M. Escher, M. Merkel, and C. M. Schneider, *A New Nanospectroscopy Tool with Synchrotron Radiation: NanoESCA@Elettra*, e-Journal of Surface Science and Nanotechnology **9**, 395 (2011).
- [77] S. Moser, *An experimentalist's guide to the matrix element in angle resolved photoemission*, J. Electr. Spectr. Rel. Phen. **214**, 29 (2017), URL <https://doi.org/10.1016/j.elspec.2016.11.007>.
- [78] J. Yeh, *Atomic Calculation of Photoionization Cross-Section and Asymmetry Parameters* Gordon and Breach Science Publishers, Langhorne, PE (USA) (1993).
- [79] J. Yeh and I. Lindau, *Atomic subshell photoionization cross sections and asymmetry parameters: 1 ≤ Z ≤ 103*, Atomic Data and Nuclear Data Tables **32**, 1 (1985), ISSN 0092-640X, URL <https://www.sciencedirect.com/science/article/pii/0092640X85900166>.
- [80] K. S. Siow, L. Britcher, S. Kumar, and H. J. Griesser, *XPS study of sulfur and phosphorus compounds with different oxidation states*, Sains Malaysiana **47**, 1913 (2018).
- [81] R. Franke, T. Chassé, P. Streubel, and A. Meisel, *Auger parameters and relaxation energies of phosphorus in solid compounds*, Journal of Electron Spectroscopy and Related Phenomena **56**, 381 (1991).
- [82] Y. Zhou, K. He, H. Hu, G. Ouyang, C. Zhu, W. Wang, S. Qin, Y. Tao, R. Chen, L. Zhang, R. Shi, C. Cheng, H. Wang, Y. Liu, Z. Liu, T. Wang, W. Huang, L. Wang, and X. Chen, *Strong Neel Ordering and Luminescence Correlation in a Two-Dimensional Antiferromagnet*, Laser Phot. Rev. **16**, 2100431 (2022), URL <https://doi.org/10.1002/lpor.202100431>.
- [83] J. Köster, A. Storm, M. Ghorbani-Asl, S. Kretschmer, T. E. Gorelik, A. V. Krasheninnikov, and U. Kaiser, *Structural and Chemical Modifications of Few-Layer Transition Metal Phosphorous Trisulfides by Electron Ir-*

- radiation*, J. Phys. Chem. C **126**, 15446 (2022), URL <https://doi.org/10.1021/acs.jpcc.2c03800>.
- [84] V. Grasso and L. Silipigni, *Low-dimensional materials: The MPX₃ family, physical features and potential future applications*, Riv. Nuov. Cim. **25**, 1 (2002), URL <https://doi.org/10.1007/bf03548909>.